

RSC Advances



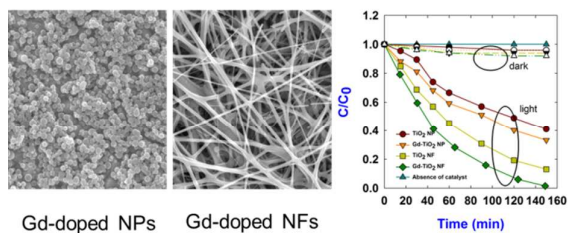
This is an *Accepted Manuscript*, which has been through the Royal Society of Chemistry peer review process and has been accepted for publication.

Accepted Manuscripts are published online shortly after acceptance, before technical editing, formatting and proof reading. Using this free service, authors can make their results available to the community, in citable form, before we publish the edited article. This *Accepted Manuscript* will be replaced by the edited, formatted and paginated article as soon as this is available.

You can find more information about *Accepted Manuscripts* in the [Information for Authors](#).

Please note that technical editing may introduce minor changes to the text and/or graphics, which may alter content. The journal's standard [Terms & Conditions](#) and the [Ethical guidelines](#) still apply. In no event shall the Royal Society of Chemistry be held responsible for any errors or omissions in this *Accepted Manuscript* or any consequences arising from the use of any information it contains.

Table of Contents



Demonstration of the role of electrode geometry on in-situ Gd-doping and their effects in the photocatalytic activity.

Cite this: DOI: 10.1039/c0xx00000x

www.rsc.org/xxxxxx

PAPER

Three-dimensional Gd doped TiO₂ fibrous photoelectrodes for efficient visible light driven photocatalytic performance†

Junghyun Choi,^{‡a} P. Sudhagar,^{‡a,b,d} P. Lakshmiathiraj,^d Jung Woo Lee,^a Anitha Devadoss,^a Sangkyu Lee,^c Taeseup Song,^c Seungki Hong,^a S. Eito,^e C. Terashima,^d Tae Hee Han,^f Jeung Ku Kang,^g A. Fujishima,^d Yong Soo Kang^{*a,b} and Ungyu Paik^{*a}

Received (in XXX, XXX) Xth XXXXXXXXX 20XX, Accepted Xth XXXXXXXXX 20XX

DOI: 10.1039/b000000x

To elucidate the influence of electrode geometry on photocatalytic performance of TiO₂, herein, we report the synthesis of three dimensional in-situ Gd-doped TiO₂ nanofibers (TiO₂-NFs) using simple electrospinning technique. The as-spun pristine TiO₂-NFs show higher photocatalytic (PC) activity (k=0.013 m⁻¹) than TiO₂ nanoparticles (TiO₂-NPs) (k=0.006 m⁻¹) electrode, which could be attributed to the fast electron transport in 1D NFs. In addition, Gd-doped TiO₂-NFs show nearly five-fold enhancement in PC degradation rate due to synergistically higher electron transport and production of HO[•] due to the effects of morphology and doping, respectively. In striking contrast, Gd-doping has no influence on PC activity of TiO₂-NPs due to increased grain boundaries, signifying the vital role of electrode architecture. The mechanism of Gd doping in pure anatase TiO₂ is investigated using density functional theory (DFT) calculations. The influence of Gd doping and the electrode architecture on the charge recombination and flat band potential variation in TiO₂ are discussed elaborately using the ultraviolet photoelectron spectroscopy (UPS) and Mott-schottky analysis and the implications of these findings for designing doped 3D fibrous photoelectrodes are discussed.

1. Introduction

Photocatalytic degradation of organic pollutants from water has gathered a great deal of interest as it utilizes renewable solar energy and produces nontoxic by-products during the reaction.¹ On this note, several semiconductor materials including ZnO, SnO₂, WO₃, α-Fe₂O₃, and TiO₂ have been widely investigated.²⁻⁴ Among them, TiO₂ is considered as the most popular and promising catalyst due to its low cost, non-toxicity, chemical & biological inertness, high photocatalytic (PC) efficiency, and photostability.⁵ Nevertheless, the large band gap of TiO₂ (3.2 eV) absorbs the light only from the ultraviolet (UV) region (under 385 nm), which results in limited PC application since only 3.0-5.0% of the incoming solar energy is utilized.⁶ Several attempts have been made to enhance the optical response of TiO₂. Doping with metal ions (Fe,⁷ Ni,⁸ V,⁹ and Cr¹⁰), non-metallic elements (N,¹¹ S,¹² and C¹³) and inducing defects in crystallite lattice^{14, 15} have been proposed as an efficient approach to tune the band gap energy of TiO₂. Recently, it is shown that the incorporation of lanthanides into the TiO₂ matrix could modify the electronic structure and optical properties of TiO₂, and thus improves the PC performance.⁵ It is reported that gadolinium¹⁶ doping would enhance the PC efficiency of TiO₂ due to the high adsorption capacity, half-filled electronic configuration, and the larger red shift.¹⁷ On the other hand, engineering the electrode surface area also

significantly influences the PC efficiency of TiO₂, as the degradation of organic pollutant takes place mostly at the electrode surface. Therefore, nanomaterials with very high surface area are considered to be effective for the PC applications than micron-size materials.¹⁸⁻²⁰ The nanostructured electrodes provide more adsorption sites for organic pollutants owing to their larger surface area and increase the light scattering sites that reduce loss from reflection by the complex internal structure. Among different nanostructures, one dimensional (1D) nanostructures offer more effective channels for electron transport due to the reduced junctions and grain boundaries compared to spherical nanocrystals. Such fast electron transport decreases the rate of recombination,²¹ which affects the PC degradation performance. However, there are no clear reports on the dominant factors influencing the PC decomposition of dye. Thus, understanding the effect of electrode geometry & doping on the PC dye degradation efficiency is critical to exploit the nanomaterials in its fullness.

Here, we report a detailed and systematic study of the electrode morphology and doping on the PC degradation through experimental and theoretical analysis. This study could yield a wealth of information on the dominant factors governing the PC degradation efficiency of the electrodes. To demonstrate the role of electrode morphology and doping on the PC activity of electrodes, undoped and Gd-doped TiO₂ nanoparticles (TiO₂-NPs) and nanofibrous (TiO₂-NFs) electrodes were prepared using

sol gel route via hydrolysis-condensation process²² and electrospinning process, respectively and their effect on the optical, chemical and PC dye degradation properties were investigated in detail. In addition, we investigate in detail the mechanism of Gd doping in TiO₂ matrix using density functional theory (DFT) calculations and address the structural benefits of the electrodes in accommodating the Gd-dopants and their consequences on the PC degradation. Also, the synergistic effects of Gd doping and the electrode architecture on the charge recombination and flat band potential variation in TiO₂ are discussed elaborately using the ultraviolet photoelectron spectroscopy (UPS) and Mott-schottky analysis.

2. Experimental

2.1 TiO₂ and Gd-doped TiO₂ nanofibers

Electrospun NFs were fabricated as follows. 0.75 g of titanium isopropoxide (97 %, Sigma Aldrich) was dissolved in 5 mL of N,N-Dimethylformamide (99.8 %, Sigma Aldrich). After stirring for 20 min, 0.3 g of acetic acid (99.5 %, Samchun Chemical) and 1 g of poly (vinyl acetate) (Mw ~ 500,000, Sigma-Aldrich) was added and continued stirring overnight. The resulted homogeneous solution was transferred to the syringe equipped with 18-G metal nozzle. The NFs were electrospun onto the FTO substrates at a DC voltage of 20 kV with a flow of 0.2 ml/h. The distance between the substrate and nozzle was 17 cm. The electrospun nanofibers were uniaxially pressed (~ 84.4 kgf/cm²) for 10 min, followed by annealing at 450 °C for 3 h in air atmosphere. For Gd-doped TiO₂-NFs, gadolinium oxide (99.9 %, Sigma Aldrich) was mixed with the TiO₂ precursor solution by magnetic stirring prior to electrospinning. The doping amount of Gd was 0.5 %.

2.2 TiO₂ and Gd-doped TiO₂ nanoparticles

For the comparative study, pristine and Gd-doped TiO₂-NPs were prepared via sol gel process using the same solution. The solutions were casted onto FTO substrates with a doctor blade and then hydrolyzed for 4 h. Finally, TiO₂-NPs were formed after annealing at 450 °C in air atmosphere.

2.3 Materials Characterization

The morphology of TiO₂ nanomaterials is observed using a field emission scanning electron microscope (FE-SEM, JEOL JSM-7600F) and field emission transmission electron microscope (FE-TEM, JEOL JEM-2100F). X-ray photoelectron spectroscopy (XPS) is used to investigate the surface composition and chemical states of TiO₂ nanomaterials using an angular resolved electron analyzer with a monochromatic Al K α source (model Theta Probe, Thermo Fisher Scientific). The XPS experiment was carried out in a high-vacuum chamber under a base pressure of 1 \times 10⁻⁶ Torr. The emitted electrons were detected at the angles between 23° and 83°. Cls peak was used to calibrate the binding energy of all the spectra. The optical absorption spectra of the electrodes were recorded in the range 350-900 nm by a JASCO UV-Vis spectrophotometer. Photoluminescence emission was recorded using Dongwoo Optron Co. Ltd. PL spectroscopy. The samples were irradiating at ambient temperature with a HeCd laser source (IK3501R-G, 325nm). The beam width and resolution was controlled by MonoRa-750i Monochromator. The

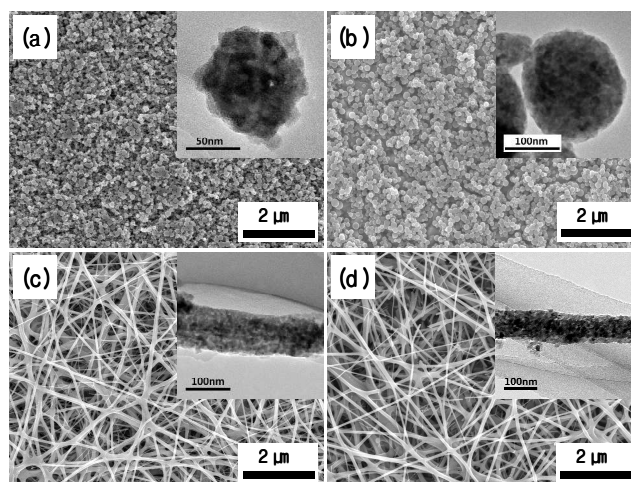


Fig.1 Scanning electron microscope (SEM) images of (a) pristine TiO₂ nanoparticles, (b) Gd-doped TiO₂ nanoparticles, (c) pristine TiO₂ nanofibers, and (d) Gd-doped TiO₂ nanofibers. Insets indicate transmission electron microscope (TEM) images of the respective electrode.

whole system equipped with a data acquisition unit (DAQ), a digitizer DAD-1602U, and optics for guiding the excitation beam and collecting luminescence signals.

2.4 Photocatalytic activity measurements

A 300 W spot light Xe lamp with an emission of $\lambda > 380$ nm was used (Hayashi Watch- works Co., Ltd, Japan, LA. 410VV-3) as a source for visible light radiation. The distance between visible light source and TiO₂ photoelectrode was fixed 5 cm in the photoelectrochemical reactor. Methyl orange (MO) dye was the model pollutant used to evaluate the PC performance of the photoelectrodes. The initial concentration of MO was 100 μ g L⁻¹. The volume of MO used is 10 ml. UV-Vis spectrophotometer (Shimadzu, UV-1700) was used to analyze the concentration of MO during the course of photodegradation.

2.5 Calculations

The Gd inclusion into the TiO₂ matrix was analyzed using first principles theory calculations. The energy calculations were performed with PW91²³ method and plane wave model,²⁴ which are installed in CASTEP program. All atoms were described using Vanderbilt ultrasoft pseudopotentials²⁵ and cut off energy of 240 eV where the set of k-points used to expand the electronic wave function based on the Monkhorst-Pack scheme.²⁶ The calculations were carried out in the anatase TiO₂ primitive tetragonal structure and a Gd atom is substituted with a Ti atom in the unit cell.

3. Results and Discussion

3.1 Structure and morphology

Fig. 1 shows the scanning electron microscope (SEM) images that describe the morphological changes of TiO₂-NPs and TiO₂-NFs with Gd-doping. The size of pristine TiO₂-NPs is around 75 nm (Fig. 1(a)), whilst the Gd-doping increased the size of TiO₂-NPs to 125 nm (Fig. 1(b)). The inset transmission electron microscope (TEM) image precisely shows the dimension of individual NPs. The morphology of the electrospun TiO₂-NFs

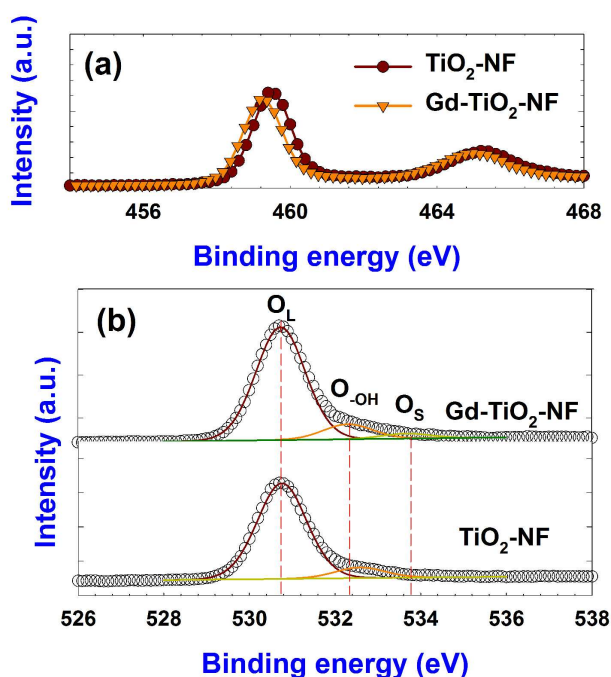


Fig.2 XPS results of (a) Ti 2p core spectra and (b) O1s core spectra of pristine and Gd-doped TiO₂ nanofibers.

and Gd-doped TiO₂-NFs is shown in Fig. 1(c) and 1(d). Contrary to the NPs system, Gd-doping shows no effect on the dimension of TiO₂-NFs, and thus resulting in NFs with a mean diameter of 100 nm with a continuous 1D nanostructure. The increased size at TiO₂ nanoparticulate structure under Gd doping may be ascribed to the possible aggregation of TiO₂ grains whereas, in the case of Gd-doped TiO₂-NFs, the predefined dimension might restrict the aggregation of TiO₂ grains. As the agglomeration of grains could indulge the active surface area of TiO₂ nanostructures, the nanofibrous electrodes are more viable and thus, anticipated to improve PC activity.²⁷ Fig. S1 (see ESI[†]) shows the high resolution TEM images of pristine TiO₂-NPs and TiO₂-NFs. Both the electrodes exhibit the same d-spacing of 3.52 Å, which corresponds to (101) plane of anatase TiO₂ (JCPDS no.21-1272). The selective area electron diffraction (SAED) patterns (Fig. S1, ESI[†]) also clearly support the presence of several characteristics planes of anatase TiO₂ include (101), (004), (200), (211), and (204). However, no changes in the crystal structure of anatase TiO₂ was observed in HRTEM images following the Gd doping and SAED patterns, which may be due to the lower doping concentration of 0.5 % gadolinium oxide. Further, the crystallite phase of pristine and Gd doped TiO₂ samples (NP and NF) has been studied with X-ray diffraction spectra (XRD), it exhibits anatase (101) phase (Figure S3) with d-spacing of 3.51 Å (JCPDS 21-1272) and is consistent with SAED observation.

3.2 Chemical environment

To investigate the influence of Gd doping on the chemical composition and chemical binding environment of TiO₂ nanomaterials, X-ray photoelectron spectroscopy (XPS) analysis was performed. Fig. 2(a) shows the Ti 2p core XPS results of pristine and Gd doped TiO₂-NFs. Two peaks are observed at

459.4 and 465.2 eV, which correspond to the signals of Ti 2p_{1/2} and Ti 2p_{3/2}, respectively, which ensure the characteristic binding energies of Ti⁴⁺ in TiO₂ matrix.²⁸ The Ti2p peak is shifted about ~0.4eV to lower binding energy infer that doping ions (Gd³⁺) were occupied in TiO₂ lattice.¹¹ Similarly, O 1s spectrum exhibits a significant difference in the intensity of the shoulder located at ~532.4 eV. Gaussian fitting was used to investigate the detailed chemical environment of oxygen atoms. The oxygen atoms in TiO₂-NFs have three possible chemical states such as lattice oxygen (530.7 eV), surface hydroxyl oxygen (532.5 eV), and surface adsorbed oxygen (533.6 eV).²⁹⁻³¹ We have estimated the chemical composition of both pristine and Gd-doped TiO₂ using the XPS results (Fig. 2). The O_H/O_{tot} ratio values are summarized in Table 1 (also see supporting information table S1).

Naldoni et al.^{32, 33} explored the influence of hydroxyl group (degree of hydrophilicity) on TiO₂ surface towards performing the pollutant mineralization. Qualitatively, the ratio of surface hydroxyl group and total lattice oxide (O_H/O_{tot}) considered as an indication of the degree of hydrophilicity.³³ In the present case, Gd-TiO₂ NF electrode showed high O_H/O_{tot} value ~ 0.17% than that of pristine TiO₂ NF. Also, the value of O_H/O_{tot} is less at Gd-TiO₂ NP (~0.13%) compare to Gd-TiO₂ NF electrodes. This may ascribe to the nature of TiO₂ electronic structures (NF or NP) which control the Gd doping quantity. From table 1, it is inferred that the occupancy of Gd doping carriers promoting hydrophilic nature of TiO₂ NF surface than TiO₂ NP. It is worth mentioning that the high degree of hydrophilicity at TiO₂-NFs is beneficial for effective adsorption of the pollutant molecule towards PC surface, which could promote the efficiency of PC degradation.³⁴

3.3 Optical property

To evaluate the optical response of TiO₂ nanomaterials in the visible light range, UV-Vis absorption and reflectance spectra were obtained as shown in Fig. 3 and Fig. S4. The absorption band edge of TiO₂-NPs is ~350 nm which is in the UV region. As anticipated, Gd doping shifts the absorption band edge of TiO₂-NPs to 445 nm. This red shift is due to the transition of electron from the valence band to the doping energy level, which is well consistent with the previous reports on doping of rare earth elements into the TiO₂ matrix.³⁵ In the case of TiO₂-NFs, it exhibit higher absorbance over the whole wavelength range than TiO₂-NPs. This can be attributed to the structural contribution of 1D nanostructure. Interestingly, from Fig. S4, NFs show higher reflectance than NPs (<500nm), indicating an enhanced light scattering in visible wavelength range, which originate from complex inner structure of 1D TiO₂-NFs leading to an increased light absorption.³⁶ Furthermore, Gd-doped TiO₂-NFs exhibit the maximum absorbance in both UV and visible range compared to other TiO₂ nanomaterials.

Table 1 Elemental composition (atomic %) of Ti and O_H/O_{tot} in pristine and Gd-doped TiO₂ nanofiber electrodes.

Electrode	Ti	O _H /O _{tot}
TiO ₂ NF	22.3	0.11
Gd-TiO ₂ NF	21.4	0.17
TiO ₂ NP	21.5	0.11
Gd-TiO ₂ NP	21.2	0.13

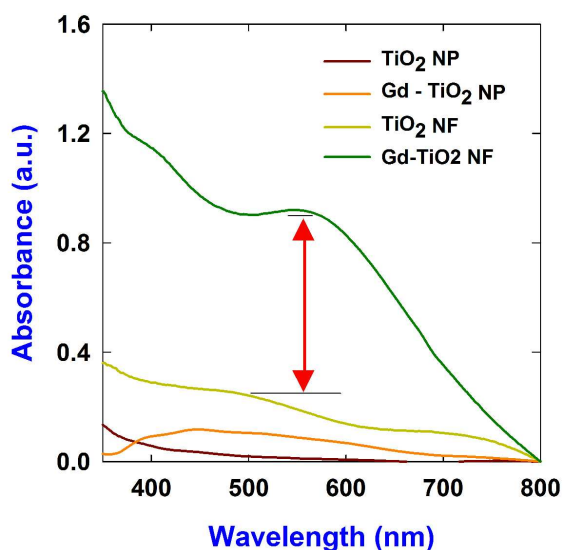


Fig.3 (a) Optical absorption spectra of pristine and Gd-doped TiO₂ nanofibers and nanoparticle electrodes.

3.4 Photocatalytic property

The photocatalytic properties of TiO₂ nanomaterials were evaluated with methyl orange (MO) dye, a universal indicator, for PC degradation. TiO₂ electrodes were prepared on the FTO glass. The thickness of pristine and Gd-doped TiO₂-NPs electrode was found to be 3.7 and 3.3 μm, respectively. The electrodes were placed in aqueous MO solution with an initial concentration of 100 μg L⁻¹. The decrease in the concentration of MO during the course of photocatalysis process under visible light irradiation is given in Fig. 4. The rate of PC degradation of MO found to follow the pseudo first order rate kinetics and the corresponding rate constant (*k*) values of MO degradation on different electrodes are given in Table 2. In the absence of catalyst, MO is stable under visible light irradiation and after introducing TiO₂ nanostructured electrodes the PC degradation rate of MO increased monotonically as a function of electrode performance. Among the electrodes, pristine TiO₂-NPs and Gd doped TiO₂-NPs electrode exhibited the lowest PC efficiency (0.006 m⁻¹). It indicates that the doping of Gd into TiO₂-NPs matrix did not influence the photo degradation of MO. This is attributed to the poor distribution of Gd dopants in TiO₂-NPs surface due to agglomeration and increased grain boundaries (Fig. 1(b)). Thus, the NPs electrode acts as electron hole combination centre rather than hole trapping centre. Conversely, the rate of degradation of MO at TiO₂-NFs electrode is comparatively higher than that of pristine and Gd-doped TiO₂-NPs electrodes. The multiple light scattering effects at 1-D fibrous channel (Fig 3(b)) contributes to the visible light activity (red light photons) of 1-D TiO₂-NFs electrodes which promotes the PC degradation rate of MO to two fold (0.0134 m⁻¹) compared to nanoparticles counterpart. Furthermore, the Gd doping found to be effective in enhancing the PC property of TiO₂-NFs electrode, and resulted in nearly 99% degradation of MO within 150 min of photocatalysis with the rate constant value of 0.026 min⁻¹ which is one fold higher than that of TiO₂-NFs electrode performance. Thus, the synergistic effects of Gd-doping coupled with the morphological benefits of TiO₂-NFs results in fivefold enhancement in the PC

Table 2. Rate constant (*k*) for PC degradation of MO dye at different electrodes.

Electrodes	<i>k</i> (m ⁻¹)	R ²
TiO ₂ -NPs	0.006	0.98
Gd-doped TiO ₂ -NPs	0.006	0.98
TiO ₂ -NFs	0.013	0.99
Gd-doped TiO ₂ -NFs	0.026	0.96

degradation of MO than that of TiO₂-NPs electrode counterparts. This endorses the superior performance and feasibility of NFs electrodes than NPs structures for doped photoelectrodes. The physical adsorption of organic molecules on catalytic surface has been studied in dark condition (circled portion in dark), which shows that Gd-TiO₂ NF electrode have more MO loading than that of other electrodes. This may attributed to high degree of hydrophilicity as is discussed in table 1.

50

3.5 Electronic interfaces

The PC degradation process generally includes charge separation, charge transport, and charge recombination. It is well reported that the external doping carriers often control the electron-hole separation at host semiconductor electrodes.³⁷⁻³⁹ Therefore, in order to further decipher the influence of Gd doping carriers at different TiO₂ nanostructures, we have studied their charge recombination nature through photoluminescence (PL) spectra (without electrolyte) and the results are presented in Fig. 5(a). PL spectra provide more information on the kinetics of photocatalytic degradation.⁴⁰ Typically, lower intensity of PL emission spectrum indicates less recombination of excited electrons and holes which means good affordability to PC degradation.^{41,42}

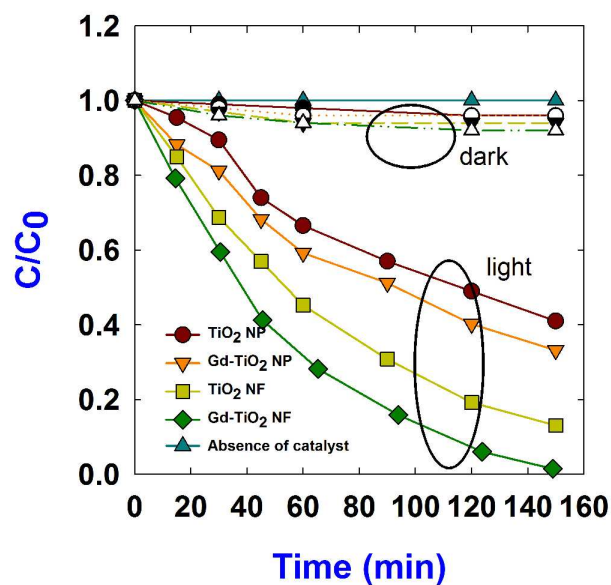


Fig.4 Normalized photocatalytic dye degradation response of pristine and Gd-doped TiO₂ nanoparticles and nanofibers electrodes. The electrodes were irradiated under visible light irradiation. The initial concentration of methyl orange was 100 μg L⁻¹.

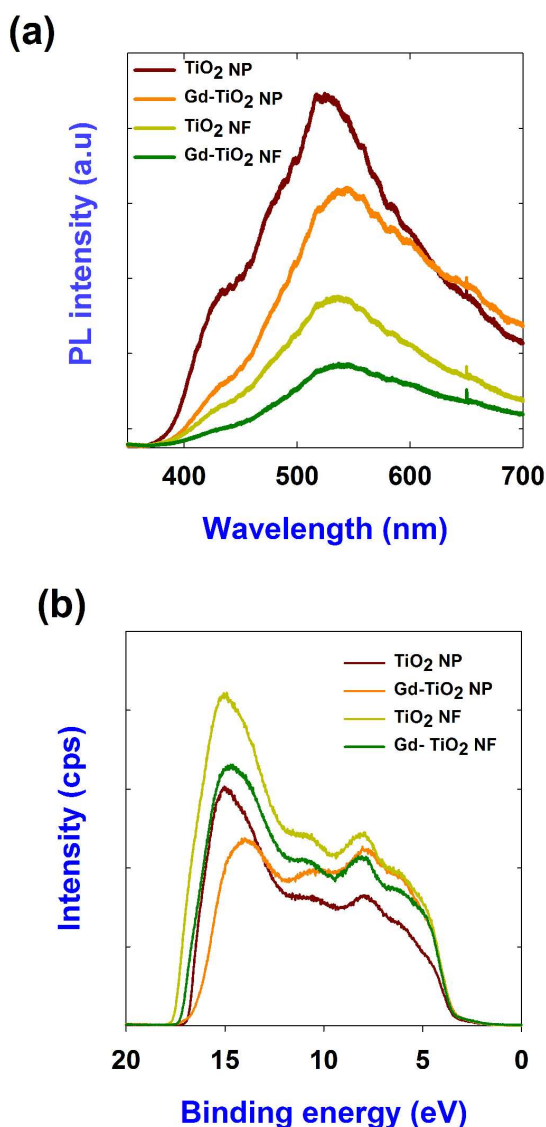


Fig.5 (a) PL emission spectra of pristine and Gd-doped TiO₂ nanostructures excited at 325 nm and (b) ultraviolet photoelectron spectra (UPS) of pristine and Gd-doped TiO₂ nanostructures.

From Fig. 5(a), it is found that the intensity of pristine TiO₂-NFs is remarkably lower than the NPs counterpart, which implies that electron-hole separation is apparently higher at fibrous electrode. This could be attributed to the reduced grain boundaries at TiO₂-NFs electrode where recombination sites were lowered and thus facilitates the interfacial electron transfer to electrolyte.⁴³ On the other hand, the Gd-doped fibrous electrodes show much lower PL emission intensity compare to pristine TiO₂-NFs. This demonstrate that the presence of Gd ions could act as an effective electron scavenger to trap the TiO₂ conduction band electrons and thus controlling the surface recombination (e⁻ and h⁺) to a larger extent⁴⁴ and hence promoting the PC degradation rate. The observed high charge separation nature at Gd doped TiO₂-NFs electrode strongly supports and enhanced PC degradation performance on their surface and is in good agreement with Fig. 4. Gd-TiO₂-NPs electrode showed high PL intensity than that of

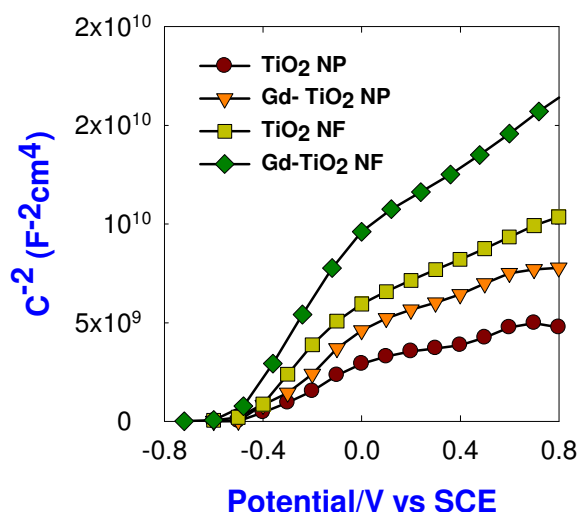


Fig.6 Mott-Schottky plots for bare and Gd doped TiO₂ nanostructures.

Gd-TiO₂-NFs which clearly implies the poor PC degradation performance. This can be attributed to the agglomeration of TiO₂ material which inturn increases the recombination rates.

It is significant to analyze the origin of observed disparity in the performance of Gd-doped TiO₂-NFs electrode with Gd-doped TiO₂-NPs electrode and their role in electronic interface of TiO₂/MO electrolyte. One simple way to analyze the interfacial charge transfer is to study the work function of the pristine and doped semiconductors. Therefore, the work functions of these systems were estimated using ultraviolet spectroscopy (UPS). The UPS spectra of pristine and Gd doped TiO₂-NPs and TiO₂-NFs electrodes are presented in Fig. 5(b). The work function of each electrodes were estimated using the following equation¹¹

$$\phi = h\nu - E_{FE} - E_{onset} \quad (1)$$

where, $h\nu = 21.2$ eV (He I source), E_{onset} is the onset of the secondary emission, and E_{FE} is the Fermi edge. The onset of the secondary emission (E_{onset}) was determined by extrapolating two solid lines from the background and straight onset. The estimated onset of the secondary emission, valence band maximum (VBM) and work function values are presented in Table S1 (See supporting information). From table S2, the work functions of TiO₂-NFs and Gd-doped TiO₂-NFs were calculated to be 3.6 and 3.96 eV, respectively and for TiO₂-NPs and Gd-doped TiO₂-NPs is 4.32 and 4.50, respectively. The shift in work function ($\Delta\phi_n$) under Gd doping is higher at NFs electrodes ($\Delta\phi_n = 0.36$ eV) compare to NPs electrodes ($\Delta\phi_n = 0.18$ eV). The high work function shift in NFs electrodes indicates that the occupancy of Gd³⁺ carriers is effective below the conduction band of TiO₂-NFs framework and hence lowers the minimum. Such significant variation in conduction band minimum (CBM) indicates a positive shift in the flat band potential (V_{fb}) with respect to a normal hydrogen electrode (NHE).⁴⁵ The positive shift indicates the production of large number of HO•, which is favorable for water detoxification.

3.6 Influence of Gd doping at TiO₂ lattice

The role of Gd doping on flat band potential of TiO₂ nanostructures were investigated by Mott-Schottky plots. The MS

plots were obtained by impedance spectroscopy and results are presented in Fig. 6 and the extrapolation of Mott-Schottky plots (C^2 vs E , electrode potential) were extracted using the following equation and flat band potential can be estimated^{16, 46}

$$\frac{1}{C^2} = \frac{2}{N_D \cdot \epsilon_0 \cdot \epsilon_{TiO_2} \cdot e} \left(E - E_{fb} - \frac{kBT}{e} \right)$$

where C is the space charge capacitance, E the externally applied potential, E_{fb} the flatband potential at semiconductor/electrolyte junction, N_D the donor density, ϵ_0 the permittivity of the free space, ϵ_{TiO_2} the permittivity of the semiconductor electrode, e the elementary charge, k_B the Boltzmann's constant, and T the operation temperature. Compared with bare TiO_2 -NFs electrodes, the E_{fb} of Gd doped TiO_2 -NFs electrode shifted to -0.06V negatively which imply that a higher quasi-Fermi level could be obtained by doping Gd.⁴⁶ In the case of TiO_2 -NFs electrodes there is no such significant E_{fb} variation is observed. From the MS plots, it is clearly understood that Gd doping is apparently effective in NFs electrodes compare to NPs electrode. The observed E_{fb} shift at Gd doped TiO_2 -NFs electrodes were in line with the UPS results. These results provide significant new insights into the differences between materials with rare-earth dopants optimized for NFs and NPs based photoelectrodes as well as choice of doping technique.

Inherently, TiO_2 -NFs structure pertain high quantity of anatase (001) crystallite planes compared to nanoparticulate.⁴⁷ According to 'Lanthanide contraction' law, these c-axis lattice sites at TiO_2 are more favorable for altering their electronic structure under Gd ion doping.⁵ Mostly, Gd doping carriers may replace the Ti sites rather Ti-O sites and form $Ti_{1-x}Gd_xO_2$. This speculation has been testified by DFT calculation and simulated results are presented in Fig. 7. After the full optimization of anatase TiO_2 primitive cell, the lattice parameters were $a = b = 3.794 \text{ \AA}$, $c = 9.945 \text{ \AA}$ and $\alpha = \beta = \gamma = 90^\circ$. The Ti atom, existing in the octahedral site of the unit cell, has bonding length as 1.958 Å in xy-plane and as 2.003 Å along z-axis with neighbouring O atoms, which is shown in the Fig. 7(a). The inner stress of the cell is -0.047 GPa, and also the Cartesian components of the stress tensors are presented in the Table S3 (see supporting information).

To investigate Gd doping effect into the TiO_2 lattice, the Ti atom at the octahedral site in the unit cell was substituted by Gd atom. Remarkably, the bonding length of Gd atom and neighbouring O atoms ranges from 2.071 to 2.486 Å (Fig. 7(b)). This might be due to larger atomic radius of Gd compared to Ti. Furthermore, the inner stress of the cell is 23.688 GPa that is 500 fold higher pressure than that of pure TiO_2 cell, leading to large distortion of the lattice. This phenomenon coincides well with the previous report by Zhao *et al.* that lanthanide doping in the TiO_2 matrix is thermodynamically unfavorable.⁵ From Fig. 7(b) and Table 4, it infers that the electronic structure of TiO_2 is contracted by occupancy of lanthanide ions. The analogous contracted (001)

Table 3 Cartesian components of stress tensor of Gd³⁺ doped TiO_2 lattice

Cartesian components (Gpa)			
	x	y	z
x	-22.761816	0.446653	0.946477
y	0.446653	24.956437	0.396816
z	0.946477	-0.396816	-23.345599

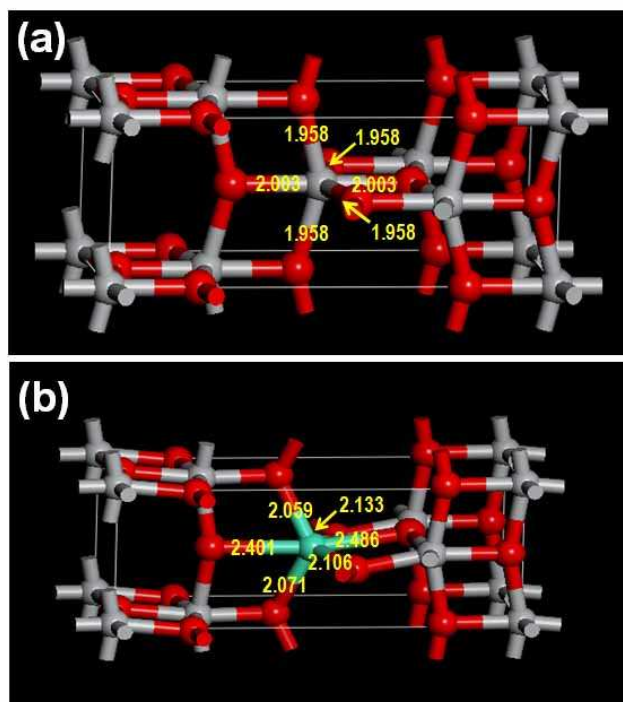


Fig.7 Optimized structures of pristine TiO_2 and Gd-doped TiO_2 . (Numbers in yellow are the bonding length of Ti (or Gd) and neighboring O atoms)

TiO_2 lattice crystallite structures under foreign atom (N ion) occupation was well studied.^{48, 49} It is reported that the lattice distortion by foreign atom in TiO_2 lattice significantly promotes dipole moment of the crystal surface through enhancing the local internal field. The high dipole moment facilitates the separation of photoexcited electron-hole pairs at their crystallite surface and markedly suppresses the charge recombination. The minimized charge recombination rate by favorable Gd doping at (001) TiO_2 fibrous crystallite sites promotes the PC degradation performance. The simulated results of Gd doped (001) TiO_2 reflect the insights of fibrous surface and are consistent with the experimental results on PC dye degradation (Table 2). However, quantitative relationship between the electronic structure modification at Gd-doped TiO_2 -NFs and the enhancement of photocatalytic activity needs further investigation.

From the above discussion, it is anticipated that the beneficial advantageous of Gd-doped TiO_2 -NFs electrodes in (a) improving visible light activity (b) high electron life time and (c) high scattering offer widespread applications as a photoanodes in photoelectrochemical energy conversion systems, dye or QDs-sensitized solar cells, and water splitting hydrogen generation.

4. Conclusion

In summary, we demonstrate a simple one-step synthesis methodology of Gd-doped TiO_2 -NFs electrode for photocatalytic degradation of organic pollutants in water. The mechanism of Gd-doping was also described using density functional theory calculations. The NF architecture results in two-fold enhancement in PC degradation rate. A combination of structural benefits of NFs and doping of Gd to TiO_2 matrix yields five-fold enhancement in the rate of PC decay of MO dye compared to the

conventional TiO₂-NPs electrode. Such remarkable enhancement in the Gd-doped TiO₂-NFs electrodes is attributed to the higher level of absorption by light scattering, fast charge transport along the TiO₂-NFs, and the retarded recombination induced by the generation of lower energy level for Gd³⁺ carriers. These results clearly indicate that Gd-doped TiO₂ fibrous architectures can be a potential candidate for efficient photocatalysis under visible light irradiation. Also, we expect that this methodology can be applied to fabricate high performance electrodes of photochemical devices.

ACKNOWLEDGMENTS

‡These authors equally contributed to this work. J.C. and P.S. conceived the research idea; J.C., P.S., P.L., E.I., S.H. performed the experiments; J.C., P.S., P.L., E.I., J.W.L., T.S., S.L. Y.S.K. and U.P. analyzed the results; J.C., P.S., A.D. Y.S.K. and U.P. wrote the paper. C.T., T.H.H., J.K. A.F., Y.S.K. and U.P. guided the experimental work.

This work was supported by the Global Research Laboratory (GRL) Program (K20704000003TA050000310) through the National Research Foundation of Korea (NRF) funded by the Ministry of Science, ICT (Information and Communication Technologies) and Future Planning, an International Cooperation program of the Korea Institute of Energy Technology Evaluation and Planning (KETEP) grant funded by the Korean Ministry of Trade, Industry & Energy (2011T100100369). This research was also supported by the Korea Center for Artificial Photosynthesis (KCAP, NRF-2012-M1A2A2671834), the Priority Research Centers Program (2011-0031407). One of the authors P.S. acknowledges the financial support from Japan Society for the Promotion of Science (JSPS) for providing a Postdoctoral Research Fellowship.

Notes and references

^a Department of Energy Engineering, Hanyang University, Seoul 133-791, Korea. E-mail: upaik@hanyang.ac.kr; kangys@hanyang.ac.kr

^b Center for Next Generation Dye-sensitized Solar Cells, Hanyang University, Seoul 133-791, Korea.

^c Department of Materials Science and Engineering, Hanyang University, Seoul 133-791, Korea.

^d Photocatalysis International Research Center, Tokyo University of Science, 2641 Yamazaki, Noda, Chiba 278-8510, Japan.

^e Flucto-Order Functions Research Team, RIKEN-ASI, Saitama 351-0198, Japan.

^f Department of Organic and Nano Engineering, Hanyang University, Seoul 133-791, Korea

^g Graduate School of EEWS, Department of Materials Science and Engineering, and NanoCentury KI, KAIST, 335 Gwahangno, Yuseong Gu, Daejeon 305-701, Korea

† Electronic Supplementary Information (ESI) available: [HRTEM images, SAED patterns, Cross sectional SEM images and XPS, UPS and DFT results]. See DOI: 10.1039/b000000x/

- S. Chakrabarti and B. K. Dutta, *Journal of Hazardous Materials*, 2004, **112**, 269-278.
- H. J. Wang, F. Q. Sun, Y. Zhang, L. S. Li, H. Y. Chen, Q. S. Wu and J. C. Yu, *J Mater Chem*, 2010, **20**, 5641-5645.
- D. Chen and J. H. Ye, *Adv Funct Mater*, 2008, **18**, 1922-1928.
- M. A. Gondal, M. N. Sayeed and A. Alarfaj, *Chem Phys Lett*, 2007, **445**, 325-330.
- Z. Y. Zhao and Q. J. Liu, *J Phys D Appl Phys*, 2008, **41**.
- A. W. Xu, Y. Gao and H. Q. Liu, *J Catal*, 2002, **207**, 151-157.
- S. George, S. Pokhrel, Z. Ji, B. L. Henderson, T. Xia, L. Li, J. I. Zink, A. E. Nel and L. Mädler, *Journal of the American Chemical Society*, 2011, **133**, 11270-11278.
- Z. Yao, F. Jia, S. Tian, C. Li, Z. Jiang and X. Bai, *ACS Applied Materials & Interfaces*, 2010, **2**, 2617-2622.
- H. Jie, H. Park, K. B. Lee, H. J. Chang, J. P. Ahn and J. K. Park, *Surf Interface Anal*, 2012, **44**, 1449-1452.
- H. Zhu, J. Tao and X. Dong, *The Journal of Physical Chemistry C*, 2010, **114**, 2873-2879.
- P. Sudhagar, K. Asokan, E. Ito and Y. S. Kang, *Nanoscale*, 2012, **4**, 2416-2422.
- Q. Sun, J. Zhang, P. Q. Wang, J. Zheng, X. N. Zhang, Y. Z. Cui, J. W. Feng and Y. J. Zhu, *J Renew Sustain Ener*, 2012, **4**.
- J. H. Park, S. Kim and A. J. Bard, *Nano Letters*, 2005, **6**, 24-28.
- A. Naldoni, M. Allieta, S. Santangelo, M. Marelli, F. Fabbri, S. Cappelli, C. L. Bianchi, R. Psaro and V. Dal Santo, *Journal of the American Chemical Society*, 2012, **134**, 7600-7603.
- X. Chen, L. Liu, P. Y. Yu and S. S. Mao, *Science*, 2011, **331**, 746-750.
- F. Fabregat-Santiago, G. Garcia-Belmonte, J. Bisquert, P. Bogdanoff and A. Zaban, *J Electrochem Soc*, 2003, **150**, E293-E298.
- Z. M. El-Bahy, A. A. Ismail and R. M. Mohamed, *Journal of Hazardous Materials*, 2009, **166**, 138-143.
- Z. Y. Liu, D. D. L. Sun, P. Guo and J. O. Leckie, *Nano Letters*, 2007, **7**, 1081-1085.
- X. W. Zhang, J. H. Pan, A. J. Du, W. J. Fu, D. D. Sun and J. O. Leckie, *Water Res*, 2009, **43**, 1179-1186.
- Z. Liu, X. Zhang, S. Nishimoto, M. Jin, D. A. Tryk, T. Murakami and A. Fujishima, *J Phys Chem C*, 2008, **112**, 253-259.
- S. Cavaliere, S. Subianto, I. Savych, D. J. Jones and J. Roziere, *Energ Environ Sci*, 2011, **4**, 4761-4785.
- J. Choi, S. Lee, J. Ha, T. Song and U. Paik, *Nanoscale*, 2013, **5**, 3230-3234.
- J. P. Perdew, K. Burke and M. Ernzerhof, *Phys Rev Lett*, 1996, **77**, 3865-3868.
- M. C. Payne, M. P. Teter, D. C. Allan, T. A. Arias and J. D. Joannopoulos, *Rev Mod Phys*, 1992, **64**, 1045-1097.
- D. Vanderbilt, *Phys Rev B*, 1990, **41**, 7892-7895.
- H. J. Monkhorst and J. D. Pack, *Phys Rev B*, 1976, **13**, 5188-5192.
- S. K. Choi, S. Kim, S. K. Lim and H. Park, *The Journal of Physical Chemistry C*, 2010, **114**, 16475-16480.
- M. You, T. G. Kim and Y. M. Sung, *Cryst Growth Des*, 2010, **10**, 983-987.
- L. Yu, S. Yuan, L. Y. Shi, Y. Zhao and J. H. Fang, *Micropor Mesopor Mat*, 2010, **134**, 108-114.
- B. F. Xin, D. D. Ding, Y. Gao, X. H. Jin, H. G. Fu and P. Wang, *Appl Surf Sci*, 2009, **255**, 5896-5901.
- P. Zhang, C. L. Shao, Z. Y. Zhang, M. Y. Zhang, J. B. Mu, Z. C. Guo, Y. Y. Sun and Y. C. Liu, *J Mater Chem*, 2011, **21**, 17746-17753.
- A. Naldoni, C. L. Bianchi, C. Pirola and K. S. Suslick, *Ultrasonics Sonochemistry*, 2013, **20**, 445-451.
- S. Ardizzone, C. L. Bianchi, G. Cappelletti, A. Naldoni and C. Pirola, *Environmental Science & Technology*, 2008, **42**, 6671-6676.
- G. Cappelletti, S. Ardizzone, C. Bianchi, S. Gialanella, A. Naldoni, C. Pirola and V. Ragaini, *Nanoscale Research Letters*, 2008, **4**, 97 - 105.
- B. Singhal, A. Porwal, A. Sharma, R. Ameta and S. C. Ameta, *J Photoch Photobio A*, 1997, **108**, 85-88.
- I. S. Cho, Z. B. Chen, A. J. Forman, D. R. Kim, P. M. Rao, T. F. Jaramillo and X. L. Zheng, *Nano Letters*, 2011, **11**, 4978-4984.
- R. Katoh, A. Furube, K. Yamanaka and T. Morikawa, *J Phys Chem Lett*, 2010, **1**, 3261-3265.
- S. Anandan, Y. Ikuma and V. Murugesan, *Int J Photoenergy*, 2012.
- M. Pelaez, N. T. Nolan, S. C. Pillai, M. K. Seery, P. Falaras, A. G. Kontos, P. S. M. Dunlop, J. W. J. Hamilton, J. A. Byrne,

- K. O'Shea, M. H. Entezari and D. D. Dionysiou, *Appl Catal B-Environ*, 2012, **125**, 331-349.
40. M. Long, W. Cai, J. Cai, B. Zhou, X. Chai and Y. Wu, *The Journal of Physical Chemistry B*, 2006, **110**, 20211-20216.
- 5 41. J. G. Yu, H. G. Yu, B. Cheng, X. J. Zhao, J. C. Yu and W. K. Ho, *J Phys Chem B*, 2003, **107**, 13871-13879.
42. N. Lakshminarasimhan, E. Bae and W. Choi, *J Phys Chem C*, 2007, **111**, 15244-15250.
43. H. P. Li, W. Zhang, B. Li and W. Pan, *J Am Ceram Soc*, 2010, 10 **93**, 2503-2506.
44. M. Zalas and M. Laniecki, *Sol Energ Mat Sol C*, 2005, **89**, 287-296.
45. R. Z. Ma, T. Sasaki and Y. Bando, *Chem Commun*, 2005, 948-950.
- 15 46. Y. D. Duan, N. Q. Fu, Q. P. Liu, Y. Y. Fang, X. W. Zhou, J. B. Zhang and Y. Lin, *J Phys Chem C*, 2012, **116**, 8888-8893.
47. S. H. Liu, L. Han, Y. Y. Duan, S. Asahina, O. Terasaki, Y. Y. Cao, B. Liu, L. G. Ma, J. L. Zhang and S. A. Che, *Nat Commun*, 2012, **3**.
- 20 48. K. S. Han, D. K. Lee, J. W. Lee, G. I. Lee and J. K. Kang, *Chem-Eur J*, 2011, **17**, 2579-2582.
49. K. S. Han, J. W. Lee, Y. M. Kang, J. Y. Lee and J. K. Kang, *Small*, 2008, **4**, 1682-1686.

25